A Practical Plateau Lake Extraction Algorithm Combining Novel Statistical Features and Kullback–Leibler Distance Using Synthetic Aperture Radar Imagery

Xin Zhou 🆔, Zhengjia Zhang, Qihao Chen, *Member, IEEE*, and Xiuguo Liu 🆔, *Member, IEEE*

Abstract—Due to wind-induced waves, dry sand, wet snow, and terrain shadows, the lake extraction from synthetic aperture radar (SAR) imagery in the Qinghai-Tibet plateau is accompanied by false alarms. In this article, a practical plateau lake extraction algorithm combining novel statistical features and Kullback–Leibler distance (KLD) using SAR imagery has been proposed. First, a mathematical description for the plateau lake surface called object-based generalized gamma distribution (OGΓD) features has been proposed, which is able to suppress the false alarms by using spatial context information as the large-scale descriptor. Second, the random forest classifier is used to train a multifeature set, including conventional texture features and OGΓD features, and output an initial labeling result. Finally, to suppress the false alarms in the initial lake extraction results, automatic postprocessing based on KLD has been used. The algorithm is tested by several experiments using Sentinel-1 SAR data, performing better than the state-of-the-art algorithms, achieving the overall accuracy of 99.54% while maintaining a false-alarm rate of 0.32%.

Index Terms—Kullback–Leibler distance (KLD), lake extraction, object-based generalized gamma distribution (OGΓD), Qinghai-Tibet plateau (QTP), synthetic aperture radar (SAR).

I. INTRODUCTION

THE Qinghai-Tibet plateau (QTP), including Pamirs-Hindu Kush-Karakorum-Himalayas, has an average elevation of more than 4000 m and an area of over than 3×10^6 km^2 in the center of Asia [1]. This broad region has the largest reservoir of perennial ice outside of the earth's polar ice sheets, which is the source of several of Asia's great rivers, including Yellow, Yangtze, Indus, Ganges, Brahmaputra, Irrawaddy, Salween, and Mekong, supplying water for more than 1.5 billion people downstream [2]. Therefore, the QTP is also known as "Asia's water tower." As one of the most significant features of QTP [3], some plateau lakes have increased significantly and even

collapsed in recent years due to climate changes [4], which might cause dramatical damage to the permafrost ecology and plateau infrastructure, such as Qinghai-Tibet railway [5]. Therefore, the methods of plateau lake extraction have received critical attention, which is the basis of lake monitoring.

Whereas manual measurement consumes abundant resources and is unable to monitor plateau lake continuously, the remote sensing technique offers feasible alternative approaches that overcome these constraints [6]. The passive optical sensors, including Landsat and MODIS, are the most common data used for surface-water extraction. Landsat data have been available since 1972 for mapping surface-water extent [7], which has a long archive, free of charge, and has a medium resolution about 30 m [8]. Although the spatial resolution of MODIS products is coarse, huge advantages in extensive coverage and frequent observation provide more opportunities for surface-water mapping [9]. The normalized difference water index (NDWI) and modified NDWI are commonly used to delineate water from nonwater with the optical imagery [10], [11]. However, suffering from illumination and weather conditions, it is a great challenge for optical sensors to obtain lake areas with higher time resolution.

Synthetic aperture radar (SAR), which is an active microwave sensor with broad coverage, high resolution, and continuous imaging capability, has been applied in plateau lake extraction [12]–[14]. Currently, there are three types of methodologies for water land separation using SAR images, including threshold-based, segmentation-based, and classification-based. Because the water surface is easily distinguishable in SAR images with the specular reflectance, the threshold-based methods obtain the optimal threshold by the difference between the land and water on the histogram, which are frequently used due to simplicity and efficiency, such as Otsu [15] and valley-emphasis [16]. Nonetheless, many factors, such as wind-induced waves [17], dry sand and wet snow [18], and terrain shadows [19] have an impact on extraction, resulting in a high false-alarm rate. Recently, by using context information, active contours models (ACMs), including parameter ACMs [20], and geometric ACMs [21]–[23], have widely applied in water surface delineation, which provide smooth and closed boundary contours. However, complicated calculations and massive time consuming reduce the availability of segmentation-based algorithms in large-scale lake extraction.

The classification-based algorithms, combining feature sets, and machine learning classifiers, identify the categories of each pixel or object. Although effective classifiers such as classification and regression tree [24] and random forest (RF) [25] help achieve better results, a practical feature set is equally crucial. The texture features such as the gray-level co-occurrence matrix (GLCM) features [26], [27], and local Moran's index (LMI) feature [28] were used in water extraction, combining with SVM and unsupervised algorithm, respectively. However, the features mentioned above only achieve a small-scale description for SAR images, which are susceptible to the mountain shadows or wind-induced water waves, leading to misclassifications and false alarms.

On the other hand, the postprocessing approaches are commonly used in lake extraction to deal with the resources of misclassifications and false alarms, including terrain shadows [29], false edges related to isolated targets [22], and seasonal rivers [30]. Due to the complex environment of the QTP, a comprehensive and effective solution to false alarms is needed. One possible solution is to postprocess the results of the initial classification using some statistical distance or metrics, which can describe the distance between two distributions without being affected by a small amount of noise. Several metrics, like the posterior probability of the region's mean [31], minimum stochastic distance [32], and Kullback–Leibler distance (KLD) [33], have been reported. For two regions modeling by the generalized gamma distribution (GΓD), the KLD is more suitable than others to measure the similarity between them.

In this article, a practical plateau lake extraction algorithm combining novel statistical features named object-based GΓD (OGΓD) and KLD using SAR imagery is proposed, solving the high false-alarm rate from two aspects. Aim at achieving the large-scale description of lake surface using spatial context information, the new proposed OGΓD features, which is based on scale-adaptive segmentation and two parameters of GΓD, are combined with conventional texture features. Meanwhile, a postprogress step using KLD between initial label regions is introduced to deal with false alarms and misclassifications of initial classification results. Unlike the features that participate in the initial classification, KLD postprocessing considers spatial context information using the initial classification results.

II. STUDY AREA AND DATA

The Hoh Xil region, which is the so-called "No man land," is located in the hinterland of the QTP, between 33°30'–36°29' N and 81°56'–94°06' E, with an area of about 2.35×10^5 km². In this region, lakes distribute densely, including 107 lakes with an area above 1.0 km², and most of them are endorheic lakes. Eight lakes, including Zhuonai lake, Yanhu lake, Haidingnuoer lake, Telashi lake, Kekexili lake, Cuodarima, Duoergaicuo, and Kekao lake, are chosen in this study. These lakes have expanded rapidly due to climate change and even collapsed in recent years. For instance, Zhuonai lake outburst on September 15, 2011, a large amount of water discharge flew the downstream Yanhu lake, causing significant expansions of lake area. Yanhu lake has increased more than 30 km² in the following year and continued
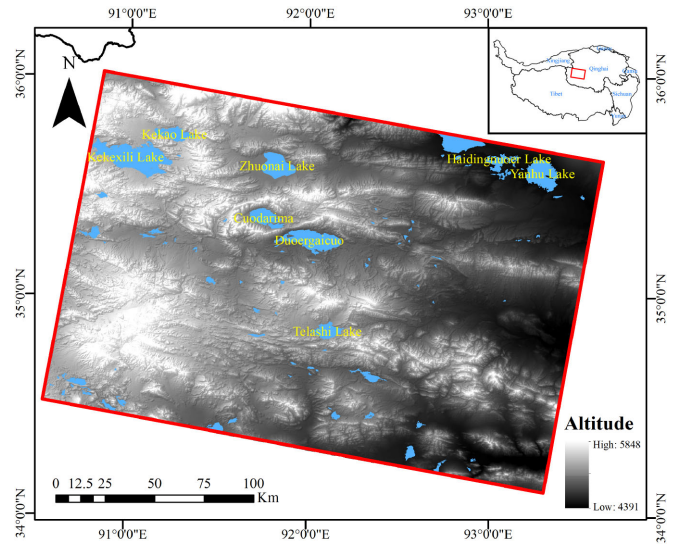

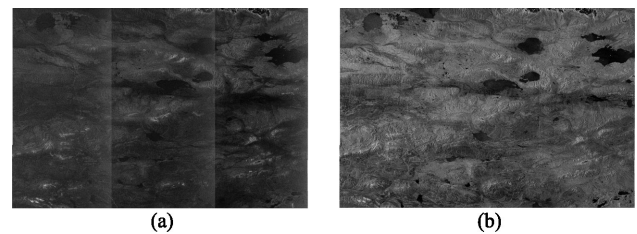Fig. 1. Map of the study area in the Hoh Xil region.

Fig. 2. Sentinel-1 GRD image acquired on August 2, 2019. (a) VH polarization. (b) VV polarization.

to increase from 2012 to 2015 [34]. Recently, Liu *et al.* [35] showed that according to change trends of area and water level during 2016–2018, Yanhu lake will overflow in the next 1 to 2 years. Fig. 1 is the map of the study area in the Hoh Xil region.

The Sentinel-1 Level-1 ground range detected (GRD) SAR image at Interferometric Wide Swath (IW) mode was used for verification and analysis in this article. The resolution in both of the azimuth and range direction is 10 m. The image was acquired on August 2, 2019, and downloaded from the Scientific Data Hub supported by the European Space Agency (ESA), with a 25723×16736 size. Both copolarized (VV) and cross-polarized (VH) data were available, as shown in Fig. 2. The eight lakes mentioned previously were covered by one scene image, in the different swath.

III. METHODS

The proposed method consists of 1) preprocessing, 2) feature calculation and classification, and 3) postprocessing using a modified KLD. The complete workflow of the proposed approach is shown in Fig. 3. The high false-alarm rate of plateau lake extraction is suppressed from two aspects, including multifeatures and KLD postprocessing.
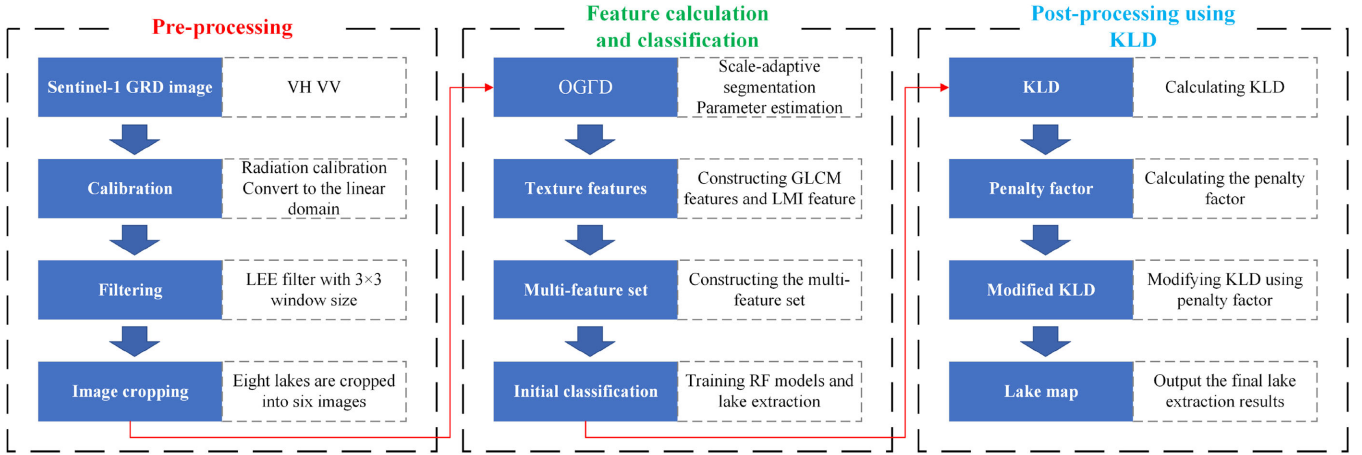
Fig. 3. Workflow of the proposed approach.

A. Preprocessing

The preprocessing includes calibration, speckle filtering, and image cropping, using the SNAP, the ENVI 5.3.1, and the SARscape 5.2.1 software packages. First, the digital number (DN) value is converted to $\sigma0$ using the following equation by the SNAP software:

$$\sigma_0 = \text{CalFactor} \times \text{DN}^2 \times \sin\theta_i \quad (1)$$

where the θ_i is the incidence angle. After calibration, SAR images need to be converted from the logarithmic domain to the linear domain for subsequent statistical modeling by GΓD, i.e., from the decibel image to the amplitude image

$$\text{I}_A = \sqrt{(\sigma_0/10)^{10}}. \quad (2)$$

In order to suppress the inherent speckle, a LEE filter with a 3×3 pixels sliding window is applied, which is a general step in SAR image preprocessing. Usually, the geocoding step is used to correct the radar coordinate system to the geodetic coordinate system. Nevertheless, geocoding will introduce geometric errors, affecting the accuracy of subsequent SAR image interpretation [22]. After filtering, the eight lakes mentioned in Section II are cropped into six images, of which one is Yanhu lake and Haidingnuoer lake, one is Duoergaicuo and Cuodarima, and the other is one each. The ground-truth graph of each lake is manually digitized by visual interpretation of the amplitude image before the quantitative evaluation of the extraction results.

B. OGΓD Features and Multifeature Set

The GΓD, a state-of-the-art empirical model, provides a novel way to express the SAR amplitude image in this study. Despite the lack of a strict physical basis, the empirical models, as purely mathematical theories, such as log-normal, Weibull, and Fisher, have been proved with an excellent performance in well-known examples. Particularly, the GΓD was used for modeling many types of clutter, not only for the extremely heterogeneous state like the urban area but also for the homogeneous state such as farm and water surface. The probability density function (pdf)

of GΓD revised in [36] is expressed as

$$p(z) = \frac{|v| \, k^k}{\sigma \Gamma(k)} \left(\frac{z}{\sigma}\right)^{kv-1} \exp\left\{-k\left(\frac{z}{\sigma}\right)^v\right\} \, \sigma, |v|, k > 0, z \geq 0 \quad (3)$$

where σ, k, and v represent scale, shape, and power parameter of the GΓD, respectively; $\Gamma(\cdot)$ denotes the gamma function. The estimators based on the method of logarithmic cumulants are shown as

$$\frac{\Psi^3\left(1, \hat{k}\right)}{\Psi^2\left(2, \hat{k}\right)} = \frac{\hat{c}_2^3}{\hat{c}_3^2} \quad (4)$$

$$\hat{v} = \text{sgn}\left(-\hat{c}_3\right)\sqrt{\Psi\left(1, \hat{k}\right)/\hat{c}_2} \quad (5)$$

$$\hat{\sigma} = \exp\left\{\hat{c}_1 - \left(\Psi\left(\hat{k}\right) - \ln\hat{k}\right)/\hat{v}\right\} \quad (6)$$

where $\Psi(\cdot)$ and $\Psi(m, \cdot)$ denote the digamma function and the mth-order polygamma function, respectively; $\text{sgn}(\cdot)$ represents the sign function; $\hat{c}_1, \hat{c}_2, \hat{c}_3$ represent the first three-order sample log-cumulants as

$$\begin{cases} \hat{c}_1 = \frac{1}{N} \sum_{i=1}^{N} \ln x_i \\ \hat{c}_2 = \frac{1}{N} \sum_{i=1}^{N} (\ln x_i - \hat{c}_1)^2 \\ \hat{c}_3 = \frac{1}{N} \sum_{i=1}^{N} (\ln x_i - \hat{c}_1)^3 \end{cases} \quad (7)$$

where N represents the number of samples participating in the estimation.

Based on the different $\hat{k}$ estimators, which are related to the ratio $\hat{c}_2^3/\hat{c}_3^2$, the corresponding $\hat{v}$ and $\hat{\sigma}$ of the GΓD are derived from (5) and (6), respectively. In (4), since the $\Psi^3(1, \hat{k})/\Psi^2(2, \hat{k})$ is a continuous monotonically increasing function, a unique minimum of 0.25 is obtained when $\hat{k}$ approaches zero. Therefore, the ratio of second-order and third-order log-cumulant must require to satisfy $\hat{c}_2^3/\hat{c}_3^2 \geq 0.25$, otherwise the estimator $\hat{k}$ would estimate fail. An approximation method for solving the problem

when $\hat{c}_2^3/\hat{c}_3^2 < 0.25$, is written as follow:

$$\frac{\hat{k}^2}{\hat{k} + \frac{1}{2}} = \frac{\hat{c}_2^3}{\hat{c}_3^2}. \tag{8}$$

In order to obtain OGΓD features, the graph-based segmentation [37] and the stepwise evolution analysis (SEA) framework [38] are employed to perform the optimal scale segmentation. In recent years, the object-based image analysis technique has widely applied in interpreting SAR images based on segmentation, showing a positive effect on speckle suppression in classification [39]. Generally, the segmentation process has two steps. First, the image is divided into nonoverlapping and separated homogeneous regions by the oversegmentation process. Then, an optimal scale parameter that determines the maximum possible variation of heterogeneity is selected for adjacent regions merging. Unfortunately, the choice of the optimal scale parameter is a significant challenge by using a trial-and-error strategy, depending on the subjective intuition. Furthermore, the meaning of the scale parameter is ambiguous in various segmentation approaches, so it is difficult to make a selection of the optimal one. To solve the ambiguity of the scale parameter, the SEA framework is introduced for automated scale parameter estimation, analyzing local variance, and Moran's indexes step-by-step. For each object, two GΓD parameters scale ($\hat{v}$) and power ($\hat{\sigma}$) are calculated. The shape parameter k is excluded because the previous study has shown that the k would be ineffective and unable to describe the real data when the third-order sample log-cumulant is close to zero [40]. In the OGΓD features extraction process, all parameters are almost self-adaptive. Therefore, the parameters setting and choice problem are avoided.

Two types of texture features containing GLCM features and LMI feature, adopted widely inland water separation in previous papers, construct the multifeature set together with the OGΓD features. The GLCM features are computed from the similarity of different pixels over a given distance using the gray level co-occurrence matrix. In this study, six GLCM features are chosen according to the previous studies [26], [27], including homogeneity, contrast, dissimilarity, entropy, angular second moment (ASM), and correlation. The GLCM and GLCM features are calculated as

$$S_d(i, j) = \frac{P_d(i, j)}{\sum_{i=1}^{K=1} \sum_{j=1}^{K} P_d(i, j)} \tag{9}$$

$$\text{Homogeneity} = \sum_{i=1}^{k=1} \sum_{j=1}^{K} \frac{S_d(i, j)}{1 + (i + j)^2} \tag{10}$$

$$\text{Contrast} = \sum_{i=1}^{k=1} \sum_{j=1}^{K} (i - j)^2 S_d(i, j) \tag{11}$$

$$\text{Dissimilarity} = \sum_{i=1}^{k=1} \sum_{j=1}^{K} |(i - j)| S_d(i, j) \tag{12}$$

$$\text{Entropy} = \sum_{i=1}^{k=1} \sum_{j=1}^{K} S_d(i, j) \ln(S_d(i, j)) \tag{13}$$

$$\text{ASM} = \sum_{i=1}^{k=1} \sum_{j=1}^{K} [S_d(i, j)]^2 \tag{14}$$

$$\text{Correlation} = \sum_{i=1}^{k=1} \sum_{j=1}^{K} \frac{(i - \mu_x)(j - \mu_y) S_d(i, j)}{\sigma_x \sigma_y} \tag{15}$$

where d is the separated distance, K is the gray level, $P_d(i, j)$ is the second-order statistical probability between two gray level i and j, $S_d(i, j)$ is the GLCM, μ_x and σ_x represent the mean value and the standard deviation of rows, and μ_y and σ_y are columns. A local Moran statistic for an observation i is defined as [28]

$$F_{\text{mor}} = \frac{x_i - \mu}{\sigma^2} \sum_{j=1}^{N} w_{ij}(x_j - \mu) \tag{16}$$

where N is the number of pixels in one observation, μ is the mean value, σ is the standard deviation, w_{ij} is the relationship between neighborhood. In this study, the w_{ij} is set as a rook case, shown as

$$W_{\text{rook}} = \begin{pmatrix} 0 & 1 & 0 \\ 1 & 0 & 1 \\ 0 & 1 & 0 \end{pmatrix}. \tag{17}$$

Finally, the LMI feature is calculated according to the expression

$$\text{LMI} = \frac{F_{\text{mor}} - F_{\text{close}}}{F_{\text{mor}} + F_{\text{close}}} \tag{18}$$

where F_{close} represents the results of morphological closing operation.

C. Postprocessing by Modified KLD

Generally, the postprocessing step has two purposes. The first is to eliminate the isolated targets in the initial classification, and the second is to eliminate false alarms or misclassified targets. For the first purpose, the isolated regions are removed by the pixel number of regions. In this article, the eliminate threshold value is set as 100, that means if a region which is less than 100 pixels, it will be removed. Not only because the isolated targets affect the interpretation, but also the too-small sample size will cause the parameter estimation of the GΓD in KLD calculation to be extremely inaccurate. For the second purpose, pixels with a slope greater than 15°, generated based on the DEM, will be masked to eliminate the impact of terrain shadows on water extraction. After that, the KLD postprocessing is used to deal with the remaining false alarms and misclassifications. The KLD, which is one of the most widely used metrics for measuring the distance between two distributions $p_1(x)$ and $p_2(x)$, defined as

$$J_D(p_1(x), p_2(x)) = \text{KL}(p_1(x), p_2(x)) + \text{KL}(p_2(x), p_1(x)) \tag{19}$$

where $\text{KL}(\cdot, \cdot)$ represents the KL divergence. In this study, the two distributions are modeling by GΓD. Thus, for the given two GΓDs with the parameters as $\{k_1, v_1, \sigma_1\}$ and $\{k_2, v_2, \sigma_2\}$, the KL divergence between $p_1(x)$ and $p_2(x)$ can be derived as

$$\text{KL}(p_1(x), p_2(x)) = A_1 + A_2 + A_3 + A_4 \tag{20}$$

where $A_1 = \ln(C_1/C_2)$, with $C_m = |v_m|k_m{}^{k_m}/[\sigma_m{}^{k_m v_m}\Gamma(k_m)]$, $m = 1, 2$, $A_2 = -k_1$, $A_3 = (k_1 v_1 - k_2 v_2)(\ln(\sigma_1{}^{v_1}/k_1) + \Psi(k_1))/v_1$, and

$$A_4 = \begin{cases} \left(\frac{\sigma_1}{\sigma_2}\right)^{v_2} \frac{k_2 \Gamma(k_1 + v_2/v_1)}{k_1{}^{v_2/v_1}\Gamma(k_1)} & \frac{v_2}{v_1} > -k_1 \\ \infty, & \text{otherwise} \end{cases}. \tag{21}$$

Similarly, the KL divergence between $p_1(x)$ and $p_2(x)$ can be derived as

$$\text{KL}(p_2(x), p_1(x)) = B_1 + B_2 + B_3 + B_4 \tag{22}$$

where $B_1 = \ln(C_2/C_1)$, $B_2 = -k_2$, $B_3 = (k_2 v_2 - k_1 v_1)(\ln(\sigma_2{}^{v_2}/k_2) + \Psi(k_2))/v_2$, and

$$B_4 = \begin{cases} \left(\frac{\sigma_2}{\sigma_1}\right)^{v_1} \frac{k_1 \Gamma(k_2 + v_1/v_2)}{k_2{}^{v_1/v_2}\Gamma(k_2)} & \frac{v_1}{v_2} > -k_2 \\ \infty, & \text{otherwise} \end{cases}. \tag{23}$$

For two GΓDs, the KLD is actually expressing the similarity between them. When the KLD is larger, the difference is larger, and the smaller the distance is, the more similar. When the category of one distribution is known, i.e., land or water, KLD can be used to measure the similarity of another unknown to the known one. For example, for an individual region in initial labeling results, if the KLD to the water is smaller than land, it is more likely to be a water region. However, there are cases where a region is water in the initial classification result, and the discrimination by the KLD is closer to the land. The category information of the region is already included in the initial classification results, which should be used in the postprocessing.

A parameter for modifying the KLD, called a KL penalty factor, is introduced in postprocessing in order to use the initial classification results and spatial information. If a region of an unknown category is surrounded by water, then the region is more likely to be water and less likely to be an island. For the initial classification results with only two categories, if it is an independent water region, the surrounding area must be land. Although for some reason, this region is judged to be water in the results of the initial classification, it is still more likely to be land from the perspective of spatial relationships. Therefore, when calculating the KLD from this region to land and water, the constraint of spatial relationship will be introduced by the KL penalty factor. This would make the region less likely to be water unless the region and land are sufficiently different.

Based on the initial classification results, the biggest water and land area are chosen to be the default reference. For an individual region in initial labeling results, the KLD from land reference (KLD_L) and water reference (KLD_W) can be calculated separately. And the KL penalty factor P_KL is shown as

$$P_\text{KL} = \frac{\text{KLD}_\text{L} + \text{KLD}_\text{W}}{2} \tag{24}$$

which is the mean value of KLD_L and KLD_L. The modified KLD (MKLD) between region and water reference is defined as

$$\text{MKLD}_\text{W} = \text{KLD}_\text{W} + P_\text{KL}. \tag{25}$$

Similarly, the MKLD between region and land reference is defined as

$$\text{MKLD}_\text{L} = \text{KLD}_\text{L} + P_\text{KL}. \tag{26}$$
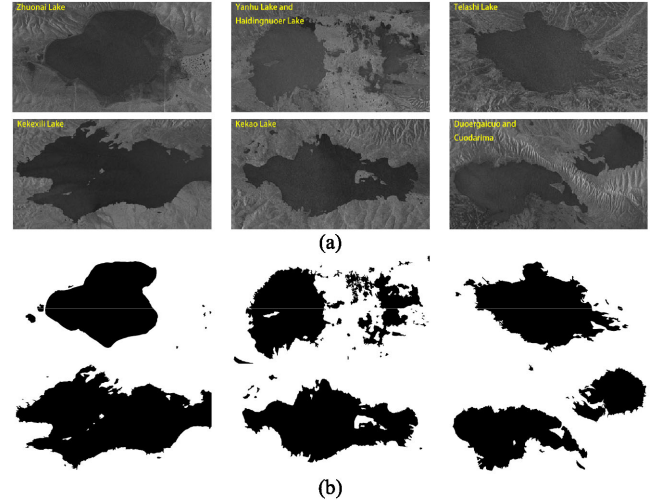
Fig. 4. Amplitude images and ground-truths graph of lakes. (a) Amplitude images in VV polarization. (b) Ground-truth graphs digitized by visual interpretation of the amplitude images.

For a region judged to be water in the initial classification, the MKLD_W and KLD_L will be compared. If $\text{MKLD}_\text{W} > \text{KLD}_\text{L}$, the region is considered to be closer to the water, and the category of this region will be changed to land. In contrast, if $\text{MKLD}_\text{W} < \text{KLD}_\text{L}$, the category of the region will not change. Similarly, for regions labeled as land in the initial classification, the MKLD_L and KLD_W will be compared to determine whether to update the category.

IV. EXPERIMENTS AND RESULTS

In order to verify the importance of OGΓD features and KLD postprocessing false-alarm suppression ability in plateau lake extraction, six SAR images with lakes were preprocessed, as shown in Fig. 4.

A. Feature Importance Evaluation

Here, four types of features were calculated for three polarization modes (VH, VV, and dual-polarization), including amplitude, GLCM features (homogeneity, contrast, dissimilarity, entropy, ASM, and correlation), LMI feature, and OGΓD features (v and σ). For the GLCM features, the window size is 15×15 in both height and width directions, which will be discussed in Section V, and the gray-level K is 64. For OGΓD features and LMI feature, the parameter setting is the default. The image with VV polarization covered Zhuonai lake was chosen to show all the features mentioned previously (see Fig. 5).

After feature calculations, all features were constructed into three types of feature images, including VH polarization (10 bands), VV polarization (10 bands), and dual-polarization (20 bands). The feature images of the dual-polarization include all features of VH polarization and VV polarization. In order to further understand the function of different features in plateau lake extraction, the RF was used for feature evaluation, which can provide the contribution of different features in the classification. The number of trees in the RF classifier was set as
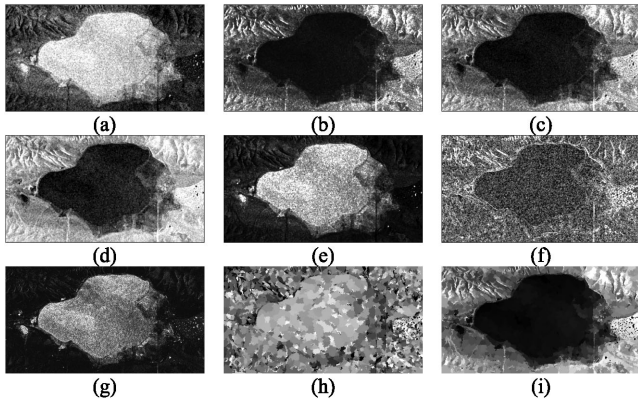
Fig. 5. Multifeatures calculated from the VV polarization amplitude image of Zhuonai lake. (a) Homogeneity. (b) Contrast. (c) Dissimilarity. (d) Entropy. (e) ASM. (f) Correlation. (g) LMI. (h) OGΓD v. (i) OGΓD σ.
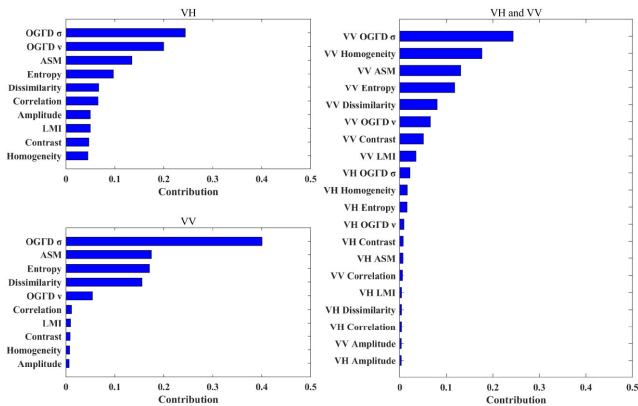

Fig. 6. Results of feature importance evaluation by the RF algorithm.

20, which will be discussed in Section V, the criterion is Gini impurity, and the max depth was set as default that means the nodes are expanded until all leaves are pure or until all leaves contain less than minimum samples split.

Fig. 6 shows the results of feature importance evaluation by the RF algorithm. In different polarizations, the feature importance ranks are different. For the VH polarization, the new proposed OGΓD σ and OGΓD v are in the top two, contributing more than 45% of the total. The next two are ASM and entropy, which are GLCM features, contribute 13.48% and 9.72%, respectively. The remaining feature contributions are all under 10%. For the VV polarization, the OGΓD σ provides an enormous contribution, approximately 40%. And the next three features contribute more than 15%, including ASM, entropy, and dissimilarity. Except for OGΓD v, the remaining features provide little contribution. For the dual-polarization, generally, the features calculated from VV polarization have a higher contribution than that of VH polarization. Among them, OGΓD σ from VV polarization provides 25% at the top of the rank. And the GLCM features from VV polarization, such as homogeneity, ASM, entropy, and dissimilarity, decrease in order. The OGΓD σ from VH polarization exceeds two VV polarization features, including correlation and amplitude, and is the most important

feature from VH polarization. In summary, OGΓD σ is essential in the extraction of plateau lakes in all three polarization modes among the ten features used in this article, while OGΓD v has a higher contribution to the extraction of lakes than other features except for OGΓD σ in VH polarization.

B. Classification by Combining Multifeatures and KLD

Three commonly used classifiers, including SVM, multilayer perceptron (MLP), decision tree (DT), and their combinations with KLD postprocessing, were chosen to verify the proposed method, which combined the RF and KLD. All of the algorithms were compared in three types of polarization modes, including VH polarization, VV polarization, and dual-polarization. The kernel was set as radial basis function in SVM classifier, and the gamma is the inverse of the number of features, 0.1 for single-polar and 0.05 for dual-polar. The MLP classifier has two hidden layers with size 20, and the activation function for the hidden layer is Relu. For all six lake images, the training samples are 20 000 points from each ground-truth graph by random generating.

All of the images of lakes were classified by four chosen methods, which were compared with the results after adding KLD postprocessing. The results of Zhuonai lake in VH polarization were shown in Fig. 7. For SVM and MLP, there are a large number of isolated speckles in the classification results, which is the primary source of false alarms, suppressed in the results of DT and RF. When the KLD postprocessing step was added to these methods, the speckles were better suppressed in the results images with the complete boundaries. Regions smaller than 100 pixels were eliminated in the postprocessing, and the remaining black spots may be thermokarst ponds slightly larger than 100 pixels. However, due to the influence of the initial classification results based on SVM and MLP, parts of the Zhuonai lake boundaries are missing, although the false alarms in them have been suppressed.

For VV polarization, overall, the classification results are better than VH polarization. The results of Yanhu lake (and Haidingnuoer lake) were chosen to show in Fig. 8. However, in the initial classification results of the four methods, there are still speckled misclassifications in the interior of the Yanhu lake. Compared with the initial classification, the results after adding KLD postprocessing have fewer speckles with pure interiors. It is hard to judge, which of the DT+KLD and RF+KLD results is better because they both have smooth boundaries and lower false alarms.

The dual-polarization results are better than the single-polar channel results, including VH and VV. Fig. 9 has shown the results of Duoergaicuo (and Cuodarima) in dual-polarization. For the initial classification results, there are a few speckles in Duoergaicuo and false alarms in the bottom left corner of the image. The KLD postprocessing eliminated a part of false alarms in the initial classification results, especially in the results of RF+KLD based.

In order to evaluate the extraction results of all lakes quantitatively, two metrics, including overall accuracy (OA) and false-alarm rate (FR), were introduced, shown as bold in
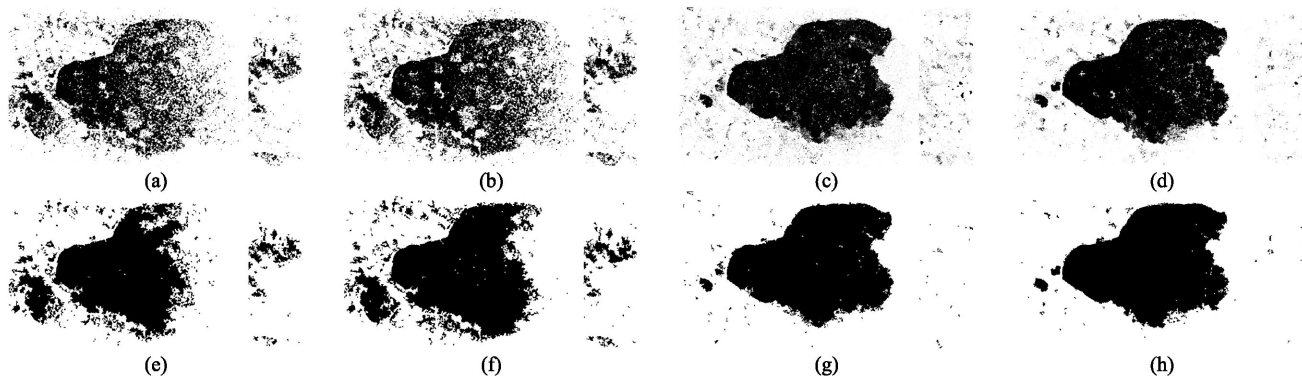
Fig. 7.   Results of Zhuonai lake in VH polarization. (a) SVM. (b) MLP. (c) DT. (d) RF. (e) SVM+KLD. (f) MLP+KLD. (g) DT+KLD. (h) RF+KLD.
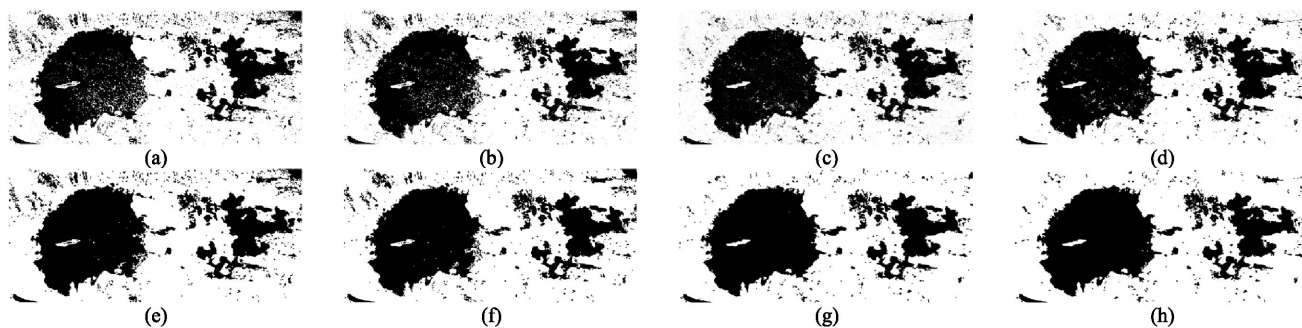

Fig. 8.   Results of Yanhu lake in VV polarization. (a) SVM. (b) MLP. (c) DT. (d) RF. (e) SVM+KLD. (f) MLP+KLD. (g) DT+KLD. (h) RF+KLD.
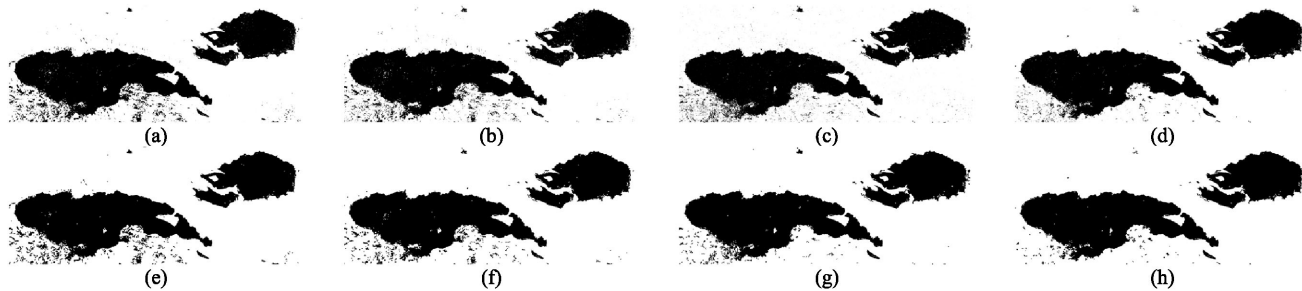

Fig. 9.   Results of Duoergaicuo in dual-polarization. (a) SVM. (b) MLP. (c) DT. (d) RF. (e) SVM+KLD. (f) MLP+KLD. (g) DT+KLD. (h) RF+KLD.

Tables I–VI. The OA factor indicates the correct rate, and FR is able to indicate false alarms. For VH polarization, the OAs of Zhuonai lake based on SVM and MLP are about 80%. The corresponding FRs are as high as 12.48% and 15.36%, respectively, suffering from speckles. Also, for Zhuonai lake, DT and RF achieved better results, with FR of 3.57% and 2.31%, respectively. Among the four methods without KLD postprocessing, RF achieved the highest of OA and lowest of FR. After KLD postprocessing, the results have improved in the increasing of OA and controlling of FR. From Tables I and II, it can be seen that in the performance of OA, more than half of the lakes based on RF+KLD are optimal. As for FR, more than half of the lowest belongs to DT+KLD, which is due to the effective suppression of false alarms by KLD postprocessing. Although

for VV polarization, the RF results are better than the other three results in the initial classification, and the DT+KLD is better than RF+KLD when KLD postprocessing was added. When using the features of two polarization channels simultaneously, RF+KLD achieved the best of OA in five lakes, except for Zhuonai lake. Meanwhile, the suppression of false alarms by RF+KLD is excellent, with five lakes below 1%.

V. DISCUSSION

A. Noise Analysis in Different Polarization

For dark targets in SAR images, such as water and oil, because their backscattering intensity may lower than the instrument sensor noise floor [41], [42], i.e., noise equivalent sigma zero

TABLE I
OA OF EIGHT METHODS IN VH CHANNEL

	SVM	MLP	DT	RF	SVM+KLD	MLP+KLD	DT+KLD	RF+KLD
Zhuonai Lake	79.07%	79.30%	94.99%	96.55%	83.34%	83.80%	98.39%	**98.40%**
Yanhu Lake	89.08%	90.99%	94.92%	96.79%	93.00%	94.09%	97.42%	**97.59%**
Telashi Lake	91.94%	92.27%	95.71%	97.19%	95.50%	95.58%	**98.46%**	98.34%
Kekexili Lake	88.41%	89.83%	90.42%	93.36%	90.17%	92.72%	94.67%	**94.90%**
Kekao Lake	98.16%	98.52%	99.01%	99.41%	98.61%	99.02%	99.45%	**99.54%**
Duoergaicuo	84.49%	87.18%	95.67%	96.26%	84.36%	87.74%	**97.37%**	97.02%

The bold figures in the Tables represent the optimal FR or OA for each lake extraction results.

TABLE II
FR OF EIGHT METHODS IN VH CHANNEL

	SVM	MLP	DT	RF	SVM+KLD	MLP+KLD	DT+KLD	RF+KLD
Zhuonai Lake	12.48%	15.36%	3.57%	2.31%	11.20%	14.08%	**1.18%**	1.33%
Yanhu Lake	7.18%	6.34%	3.82%	2.01%	5.76%	5.09%	1.70%	**1.68%**
Telashi Lake	5.25%	4.83%	3.19%	1.53%	2.99%	2.76%	**0.69%**	0.77%
Kekexili Lake	7.19%	7.37%	9.38%	5.48%	4.16%	**3.34%**	3.89%	3.65%
Kekao Lake	1.20%	0.96%	0.79%	0.42%	0.94%	0.62%	**0.32%**	**0.32%**
Duoergaicuo	10.44%	10.46%	3.05%	3.22%	11.24%	10.03%	**1.79%**	2.55%

The bold figures in the Tables represent the optimal FR or OA for each lake extraction results.

TABLE III
OA OF EIGHT METHODS IN VV CHANNEL

	SVM	MLP	DT	RF	SVM+KLD	MLP+KLD	DT+KLD	RF+KLD
Zhuonai Lake	96.51%	96.61%	98.16%	98.64%	96.95%	97.20%	**98.97%**	98.91%
Yanhu Lake	92.28%	93.43%	95.34%	96.66%	93.96%	94.68%	97.20%	**97.31%**
Telashi Lake	94.22%	94.71%	97.21%	97.90%	95.65%	96.04%	**98.51%**	98.39%
Kekexili Lake	99.27%	99.26%	99.19%	99.42%	99.40%	99.50%	99.50%	**99.57%**
Kekao Lake	98.00%	98.34%	99.13%	99.28%	97.94%	98.67%	**99.45%**	**99.45%**
Duoergaicuo	96.30%	96.51%	97.10%	97.53%	96.61%	96.85%	**97.97%**	97.95%

The bold figures in the Tables represent the optimal FR or OA for each lake extraction results.

TABLE IV
FR OF EIGHT METHODS IN VV CHANNEL

	SVM	MLP	DT	RF	SVM+KLD	MLP+KLD	DT+KLD	RF+KLD
Zhuonai Lake	3.29%	2.60%	1.32%	1.12%	3.24%	2.51%	**0.86%**	1.03%
Yanhu Lake	5.96%	5.11%	3.75%	2.47%	5.07%	4.27%	**1.90%**	**1.90%**
Telashi Lake	3.47%	3.37%	2.01%	1.41%	2.54%	2.51%	**0.67%**	1.03%
Kekexili Lake	0.31%	0.46%	0.54%	0.44%	**0.23%**	0.33%	0.29%	0.33%
Kekao Lake	2.04%	1.49%	0.61%	0.57%	2.29%	1.42%	**0.34%**	0.44%
Duoergaicuo	2.24%	2.09%	1.94%	1.58%	1.96%	1.75%	**1.12%**	1.14%

The bold figures in the Tables represent the optimal FR or OA for each lake extraction results.

TABLE V
OA OF EIGHT METHODS IN DUAL-POLARIZATION CHANNEL

	SVM	MLP	DT	RF	SVM+KLD	MLP+KLD	DT+KLD	RF+KLD
Zhuonai Lake	96.67%	96.80%	98.21%	98.70%	97.10%	97.28%	**98.98%**	98.91%
Yanhu Lake	93.97%	95.22%	96.49%	97.51%	95.18%	96.24%	97.72%	**97.89%**
Telashi Lake	95.19%	95.79%	97.36%	98.28%	96.52%	96.95%	98.68%	**98.70%**
Kekexili Lake	99.15%	99.08%	99.31%	99.43%	99.28%	99.25%	99.54%	**99.56%**
Kekao Lake	99.15%	99.23%	99.21%	99.49%	99.28%	99.39%	99.49%	**99.55%**
Duoergaicuo	95.82%	96.59%	97.37%	98.10%	96.20%	97.12%	98.21%	**98.42%**

The bold figures in the Tables represent the optimal FR or OA for each lake extraction results.

TABLE VI
FR OF EIGHT METHODS IN DUAL-POLARIZATION CHANNEL

	SVM	MLP	DT	RF	SVM+KLD	MLP+KLD	DT+KLD	RF+KLD
Zhuonai Lake	3.03%	2.59%	1.33%	0.98%	2.94%	2.52%	**0.76%**	0.97%
Yanhu Lake	4.31%	3.55%	2.46%	1.66%	3.66%	2.65%	**1.09%**	1.14%
Telashi Lake	2.83%	2.33%	1.92%	0.75%	1.64%	1.31%	0.54%	**0.41%**
Kekexili Lake	0.29%	0.36%	0.57%	0.46%	**0.20%**	0.26%	0.38%	0.39%
Kekao Lake	0.60%	0.60%	0.59%	0.35%	0.47%	0.48%	0.32%	**0.30%**
Duoergaicuo	2.87%	2.07%	1.76%	0.92%	2.50%	1.56%	0.86%	**0.59%**

The bold figures in the Tables represent the optimal FR or OA for each lake extraction results.
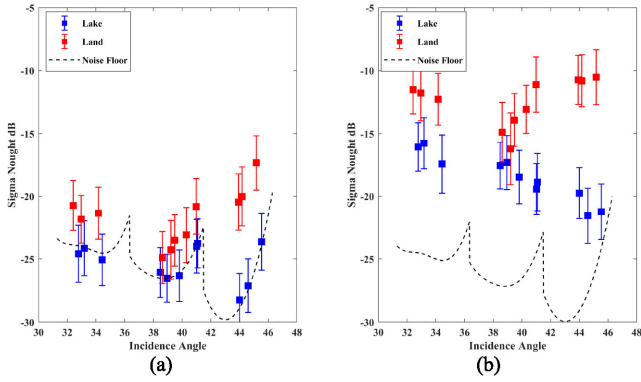
Fig. 10. Signal-to-noise analysis of each polarization channel, the vertical bars show the mean and standard deviation of the backscatter values σ_0 in (1) indicated by sample points. (a) VH polarization. (b) VV polarization.

(NESZ), their extraction accuracies are easily affected. In such a situation, the features such as the OGΓD features are no longer to accurately describe the ground objects, but the background thermal noise. For the Sentinel-1 IW mode dual-polarization product, the image may suffer crosstalk among channels and perform lower signal-to-noise ratio (SNR) [43], [44]. Hence, it is necessary to analyze the signal level in plateau lake extraction tasks based on the Sentinel-1 IW images.

For the Sentinel-1 GRD product, the NESZ can be calculated based on metadata XML file contained in each product and equations in the Sentinel-1 product specification provided by ESA. Nevertheless, both the noise metadata file and the equations are in the log domain, so the amplitude image needs to be converted back to the log domain first, i.e., decibels. Eleven sampling points with 7×7 neighborhood were selected on the lake and land, respectively, and their mean values and noise floor curve with respect to incidence angles were plotted in Fig. 10.

As shown in Fig. 10, both of the VH channel and VV channel, the boundaries of the noise floor curve between different swaths are significant. For each swath, the noise level is low in the middle and is massive on both sides. For VH polarization, the backscatter values of the lake sampling points are equal to or less than the noise floor, while the backscatter values of the land sampling points are higher than the noise floor. Therefore, the scattering characteristics of the lake have been contaminated by noise, leading to low accuracy and easily affected results when extracting lakes. In the results of VV polarization, the backscattering values of both the lake and the land are significantly higher than the noise floor, and a higher SNR ratio can provide the lake with sufficient energy to distinguish it from noise. However, it can be seen from previous experiments that the results of the VH images using the proposed method also show good performance. Furthermore, when two polarization channels are jointly used, the accuracy will be further improved, which indicates that VH polarization can provide information not included in VV polarization in the classification.

B. Estimated Window Size Selection of GLCM Features

For GLCM features, the size of the estimation window is an important parameter because it may affect the performance of
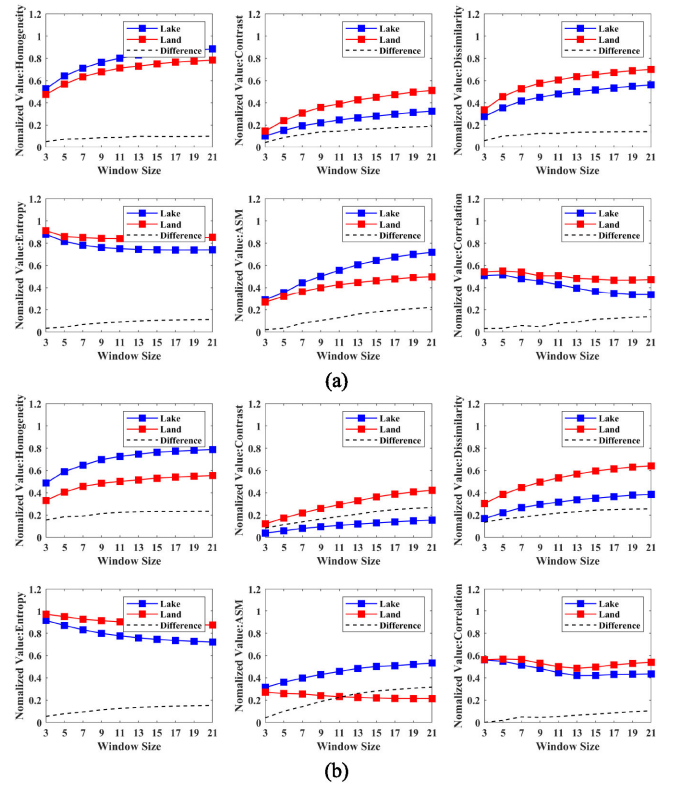

Fig. 11. Normalized GLCM feature values of lake and land, and their value differences. (a) VH polarization. (b) VV polarization.

GLCM features in the importance evaluation and the accuracy of the lake extraction. A smaller estimation window only expresses a small scale of texture features, while a larger one is easily causing the edge of the feature image to be blurred, requiring a huge calculation cost. It is necessary to obtain a practical and reliable estimation window size through experiments.

The start window size is 3 and increases by two until 21. The normalized values of the GLCM features were plotted according to different categories, as shown in Fig. 11. The black dashed line is the difference in GLCM features between the two categories. By observing the trend of the black dashed line, the optimal estimated window size will be obtained. From Fig. 11(a), for VH polarization, in the beginning, the difference between the two features increased with increasing window size. When the estimated window reached 15, this increased rate slowed down. For some features in VV polarization, such as homogeneity and dissimilarity, the changing trend, in the beginning, is relatively stable. The other features are the same as in the VH polarization. Rising speed slows down when the window size reaches 15. Although the window size increases and the difference still increases, it consumes more computing resources. Therefore, 15 is considered to be an optimal window size choice.

C. Number of Trees in the RF Classifier

The performance of the RF algorithm is not easily affected by the parameters. Generally, there is less discussion about the RF parameters. However, in the case of much noise, i.e., SAR image, some parameters of the RF may affect the results, such as
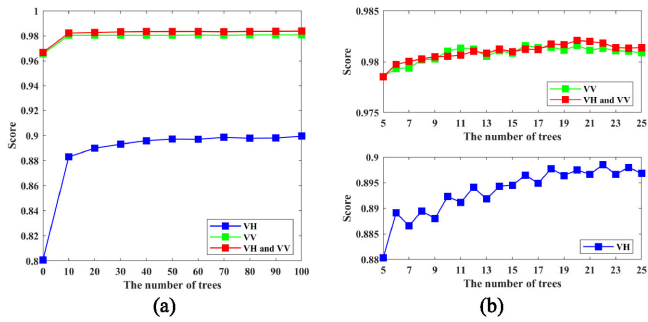
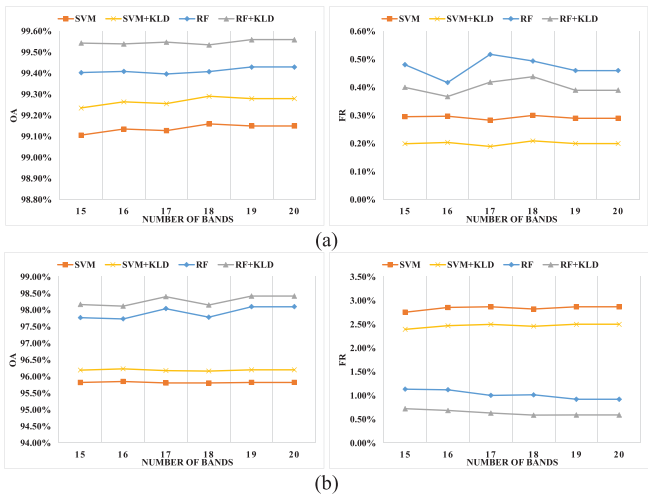Fig. 12. Two-step optimal tree number estimation scheme. (a) Rough estimation. (b) Precise estimation.

Fig. 13. OAs and FRs after band selection. (a) Kekexili lake. (b) Duoergaicuo.

the number of trees. Higher number of trees can provide a better performance but makes code slower. Thus, a property number of trees make predictions stronger and more stable.

A two-step optimal tree number estimation scheme was used with a cross-validation score, including rough estimation and precise estimation. In the rough estimation step, the tree numbers were set as 1, 10, and increase by ten until 100, as shown in Fig. 12(a). The scores rise significantly between 1 and 25 trees, and this interval was used for precise estimation. For the precise estimation, the tree number was started from 1 tree, and increase by one until 25, as shown in Fig. 12(b). In the result of VH polarization, when the number of trees reaches 20, the score of the RF model is basically stable. For VV polarization and dual-polarization, the fluctuation of the score is not obvious. Combining the results of different polarization channels, 20 is a suitable tree number choice.

D. Band Selection Analysis

For most cases, the dual-polarization has better lake extraction results than VV polarization. While for Kekexili lake and Duoergaicuo, the VV polarization using SVM and SVM+KLD

method have better results than dual-polarization. An experiment has been added to verify whether accuracy can be improved by reducing feature bands.

According to the results of RF feature importance evaluation, the least important features were removed one by one, including amplitude from VH, amplitude from VV, correlation from VH, dissimilarity from VH, and LMI from VH. Then, the OAs and FRs have been calculated, shown as Fig. 13. For Kekexili lake, from 15 to 20 features, the OAs of the four methods changed slightly, although FRs of them have a little fluctuation when combining 16 feature bands and RF. Moreover, in the results of Kekexili lake, SVM and SVM+KLD are indeed able to achieve lower FRs than RF and RF+KLD, which is different from the other five lakes. For Duoergaicuo, the OAs of RF decrease as feature bands decrease, while the OAs of SVM are unchanged. Meanwhile, the fluctuation of FRs of SVM and SVM+KLD is delicate, while the FRs of RF and RF+KLD have a little increased. By changing the number of feature bands, the OAs and FRs of the results generated by four selected algorithms changed slightly. The features in the lower order of feature importance evaluation rank may not provide further information for classification, but they also do not hinder the performance of the algorithms. Although for Kekexili lake and Duoergaicuo, the VV polarization using SVM and SVM+KLD method have better results than dual-polarization, it is better to use more features and RF+KLD that is more robust when performing plateau lake extraction in QTP.

VI. CONCLUSION

Aiming at achieving the large-scale description of plateau lakes and solving the high false alarms in the plateau lake extraction, a practical algorithm combining novel statistical features named OGΓD features and KLD has been proposed to extract shoreline of plateau lakes in the QTP, using SAR imagery. The OGΓD features, together with conventional two types of texture features, including GLCM features and LMI feature, and amplitude, were used to refine the description of the lake surface. A postprocess using the modified KLD between two regions after initial classification was used to suppress the false alarms in initial classification and improve accuracy. The proposed approach was applied to extract the lakes in the Hoh Xil region. Some conclusions can be summarized as follow.

1) The proposed OGΓD features, using the large-scale description of spatial context to suppress false alarms, was compared with the conventional texture features, including GLCM features, LMI feature, and amplitude, using RF importance evaluation. For the VH polarization, the OGΓD σ and OGΓD v are the first two important features, contributing a total of more than 45%. For the VV polarization and dual-polarization, the OGΓD σ can provide approximately 40% and 25% contribution, respectively. The results showed that OGΓD features are not only suitable for high SNR, such as VV polarization, but also for VH polarization, which is susceptible to thermal noise. At the same time, the OGΓD features provide an accurate

description for the extraction of plateau lakes, which improve the accuracy while suppressing false alarms.

2) The four classification methods, including SVM, MLP, DT, and RF, and their combination with KLD postprocessing were compared. In the results of methods without KLD postprocessing, the performance of RF in OA and FR is optimal. After combining with KLD postprocessing, the method of DT+KLD is significantly improved, which achieved results comparable to RF+KLD in single-polar channels, while the latter achieved the highest OAs and the lowest FRs in five lakes. The KLD postprocessing improves the accuracy of the four methods tested in this article and can suppress false alarms at the same time, reaching the OA of 99.54% while maintaining the FR of 0.32%.

More long-term studies involving spatial analysis of plateau lakes are needed to better understand the response of permafrost to climate warming and steadily increasing human activities. Future work to be carried out includes 1) using the polarimetric features to improve the mapping accuracy and 2) using multi-temporal data to monitor seasonal changes in the area of the lakes, compare lake expansion rates and landscape dynamics, and link the results to the meteorological records to predict the effects of future climate change in the QTP.

Reference

[1] G. Zhang, T. Yao, H. Xie, S. Kang, and Y. Lei, "Increased mass over the Tibetan Plateau: From lakes or glaciers?" *Geophys. Res. Lett.*, vol. 40, no. 10, pp. 2125–2130, 2013.

[2] W. W. Immerzeel, L. P. H. Van Beek, and M. F. P. Bierkens, "Climate change will affect the Asian water towers," *Science*, vol. 328, no. 5984, pp. 1382–1385, 2010.

[3] X. Zhou, X. Liu, and Z. Zhang, "Automatic extraction of lakes on the Qinghai-Tibet Plateau from Sentinel-1 SAR images," in *Proc. SAR Big Data Era*, 2019, pp. 1–4.

[4] J. Pei *et al.*, "Recovered Tibetan antelope at risk again," *PLoS One*, vol. 14, 2019, Art. no. e0211798.

[5] Z. Zhang, C. Wang, H. Zhang, Y. Tang, and X. Liu, "Analysis of permafrost region coherence variation in the Qinghai–Tibet Plateau with a high-resolution TerraSAR-X image," *Remote Sens.*, vol. 10, no. 2, p. 298, 2018.

[6] X. Li, D. Long, Q. Huang, P. Han, F. Zhao, and Y. Wada, "High-temporal-resolution water level and storage change data sets for lakes on the Tibetan Plateau during 2000–2017 using multiple altimetric missions and Landsat-derived lake shoreline positions," *Earth Syst. Sci. Data Discuss.*, vol. 11, no. 4, pp. 1603–1627, 2019.

[7] Y. Yang *et al.*, "Landsat 8 OLI image based terrestrial water extraction from heterogeneous backgrounds using a reflectance homogenization approach," *Remote Sens. Environ.*, vol. 171, pp. 14–32, 2015.

[8] M. G. Tulbure, M. Broich, S. V Stehman, and A. Kommareddy, "Surface water extent dynamics from three decades of seasonally continuous Landsat time series at subcontinental scale in a semi-arid region," *Remote Sens. Environ.*, vol. 178, pp. 142–157, 2016.

[9] L. Feng, X. Hou, and Y. Zheng, "Monitoring and understanding the water transparency changes of fifty large lakes on the Yangtze Plain based on long-term MODIS observations," *Remote Sens. Environ.*, vol. 221, pp. 675–686, 2019.

[10] C. S. Watson, O. King, E. S. Miles, and D. J. Quincey, "Optimising NDWI supraglacial pond classification on Himalayan debris-covered glaciers," *Remote Sens. Environ.*, vol. 217, pp. 414–425, 2018.

[11] K. V. Singh, R. Setia, S. Sahoo, A. Prasad, and B. Pateriya, "Evaluation of NDWI and MNDWI for assessment of waterlogging by integrating digital elevation model and groundwater level," *Geocarto Int.*, vol. 30, no. 6, pp. 650–661, 2015.

[12] S. Martinis *et al.*, "Comparing four operational SAR-based water and flood detection approaches," *Int. J. Remote Sens.*, vol. 36, no. 13, pp. 3519–3543, 2015.

[13] H. Vickers, E. Malnes, and K.-A. Høgda, "Long-term water surface area monitoring and derived water level using synthetic aperture radar (SAR) at Altevatn, a medium-sized Arctic lake," *Remote Sens.*, vol. 11, no. 23, p. 2780, 2019.

[14] B. Pham-Duc, C. Prigent, and F. Aires, "Surface water monitoring within Cambodia and the Vietnamese Mekong Delta over a year, with Sentinel-1 SAR observations," *Water*, vol. 9, no. 6, p. 366, 2017.

[15] A. Phan, D. N Ha, C. D Man, T. T Nguyen, H. Q Bui, and T. TN Nguyen, "Rapid assessment of flood inundation and damaged rice area in red river delta from sentinel 1A imagery," *Remote Sens.*, vol. 11, no. 17, p. 2034, 2019.

[16] P. Nakmuenwai, F. Yamazaki, and W. Liu, "Automated extraction of inundated areas from multi-temporal dual-polarization RADARSAT-2 images of the 2011 central Thailand flood," *Remote Sens.*, vol. 9, no. 1, p. 78, 2017.

[17] S. Martinis, J. Kersten, and A. Twele, "A fully automated TerraSAR-X based flood service," *ISPRS J. Photogramm. Remote Sens.*, vol. 104, pp. 203–212, 2015.

[18] M. Santoro and U. Wegmüller, "Multi-temporal synthetic aperture radar metrics applied to map open water bodies," *IEEE J. Sel. Topics Appl. Earth Observ. Remote Sens.*, vol. 7, no. 8, pp. 3225–3238, Aug. 2014.

[19] Y.-S. Song, H.-G. Sohn, and C.-H. Park, "Efficient water area classification using Radarsat-1 SAR imagery in a high relief mountainous environment," *Photogramm. Eng. Remote Sens.*, vol. 73, no. 3, pp. 285–296, 2007.

[20] A. Niedermeier, E. Romaneessen, and S. Lehner, "Detection of coastlines in SAR images using wavelet methods," *IEEE Trans. Geosci. Remote Sens.*, vol. 38, no. 5, pp. 2270–2281, Sep. 2000.

[21] M. Silveira and S. Heleno, "Separation between water and land in SAR images using region-based level sets," *IEEE Geosci. Remote Sens. Lett.*, vol. 6, no. 3, pp. 471–475, Jul. 2009.

[22] B. Tian, Z. Li, P. Tang, P. Zou, M. Zhang, and F. Niu, "Use of intensity and coherence of X-band SAR data to map Thermokarst lakes on the northern Tibetan Plateau," *IEEE J. Sel. Topics Appl. Earth Observ. Remote Sens.*, vol. 9, no. 7, pp. 3164–3176, Apr. 2016.

[23] Q. Meng, X. Wen, L. Yuan, and H. Xu, "Factorization-based active contour for water-land SAR image segmentation via the fusion of features," *IEEE Access*, vol. 7, pp. 40347–40358, 2019.

[24] L. Wang, P. Marzahn, M. Bernier, and R. Ludwig, "Mapping permafrost landscape features using object-based image classification of multi-temporal SAR images," *ISPRS J. Photogram. Remote Sens.*, vol. 141, pp. 10–29, 2018.

[25] W. Huang *et al.*, "Automated extraction of surface water extent from Sentinel-1 data," *Remote Sens.*, vol. 10, no. 5, p. 797, 2017.

[26] W. Lv, Q. Yu, and W. Yu, "Water extraction in SAR images using GLCM and support vector machine," in *Proc. IEEE 10th Int. Conf. Signal Process. Proc.*, 2010, pp. 740–743.

[27] Y. Zhang, G. Zhang, and T. Zhu, "Seasonal cycles of lakes on the Tibetan Plateau detected by Sentinel-1 SAR data," *Sci. Total Environ.*, vol. 703, 2020, Art. no. 135563.

[28] J. C. Valdiviezo-Navarro, A. Salazar-Garibay, A. Téllez-Quiñones, M. Orozco-del-Castillo, and A. A. López-Caloca, "Inland water body extraction in complex reliefs from Sentinel-1 satellite data," *J. Appl. Remote Sens.*, vol. 13, no. 1, 2019, Art. no. 16524.

[29] S. Martinis, A. Twele, and S. Voigt, "Towards operational near real-time flood detection using a split-based automatic thresholding procedure on high resolution TerraSAR-X data," *Nat. Hazards Earth Syst. Sci.*, vol. 9, no. 2, pp. 303–314, 2009.

[30] L. Wang, M. Jolivel, P. Marzahn, M. Bernier, and R. Ludwig, "Thermokarst pond dynamics in subarctic environment monitoring with radar remote sensing," *Permafrm. Periglacial Process.*, vol. 29, no. 4, pp. 231–245, 2018.

[31] Y. Wu, K. Ji, W. Yu, and Y. Su, "Region-based classification of polarimetric SAR images using Wishart MRF," *IEEE Geosci. Remote Sens. Lett.*, vol. 5, no. 4, pp. 668–672, Oct. 2008.

[32] W. B. Silva, C. C. Freitas, S. J. S. Sant'Anna, and A. C. Frery, "Classification of segments in PolSAR imagery by minimum stochastic distances between Wishart distributions," *IEEE J. Sel. Topics Appl. Earth Observ. Remote Sens.*, vol. 6, no. 3, pp. 1263–1273, Jun. 2013.

[33] X. Qin, H. Zou, S. Zhou, and K. Ji, "Region-based classification of SAR images using Kullback–Leibler distance between generalized gamma distributions," *IEEE Geosci. Remote Sens. Lett.*, vol. 12, no. 8, pp. 1655–1659, Aug. 2015.

[34] B. Liu *et al.*, "Outburst flooding of the moraine-dammed Zhuonai Lake on Tibetan plateau: Causes and impacts," *IEEE Geosci. Remote Sens. Lett.*, vol. 13, no. 4, pp. 570–574, Apr. 2016.

[35] W. H. Liu *et al.*, "Analysis on expansion trend and outburst risk of the Yanhu Lake in Hoh Xil region, Qinghai-Tibet Plateau," *J. Glaciology Geocryology*, vol. 41, no. 1, pp. 1–12, 2019.

[36] H. Li, W. Hong, Y. Wu, P. Fan, and S. Member, "On the empirical-statistical modeling of SAR images with generalized gamma distribution," *IEEE J. Sel. Topics Signal Process.*, vol. 5, no. 3, pp. 386–397, Jun. 2011.

[37] P. F. Felzenszwalb and D. P. Huttenlocher, "Efficient graph-based image segmentation," *Int. J. Comput. Vis.*, vol. 59, no. 2, pp. 167–181, 2004.

[38] Z. Hu, Q. Zhang, Q. Zou, Q. Li, and G. Wu, "Stepwise evolution analysis of the region-merging segmentation for scale parameterization," *IEEE J. Sel. Topics Appl. Earth Observ. Remote Sens.*, vol. 11, no. 7, pp. 2461–2472, Jul. 2018.

[39] Q. Xu, Q. Chen, S. Yang, and X. Liu, "Superpixel-based classification using K distribution and spatial context for polarimetric SAR images," *Remote Sens.*, vol. 8, no. 8, p. 619, 2016.

[40] G. Gao, S. Gao, K. Ouyang, J. He, and G. Li, "Scheme for characterizing clutter statistics in SAR amplitude images by combining two parametric models," *IEEE Trans. Geosci. Remote Sens.*, vol. 56, no. 10, pp. 5636–5646, Oct. 2018.

[41] S. Skrunes, C. Brekke, C. E. Jones, and B. Holt, "A multisensor comparison of experimental oil spills in polarimetric SAR for high wind conditions," *IEEE J. Sel. Topics Appl. Earth Observ Remote Sens.*, vol. 9, no. 11, pp. 4948–4961, Nov. 2016.

[42] L. Huang, B. Liu, X. Li, Z. Zhang, and W. Yu, "Technical evaluation of Sentinel-1 IW mode cross-pol radar backscattering from the ocean surface in moderate wind condition," *Remote Sens.*, vol. 9, no. 8, p. 854, 2017.

[43] P. W. Vachon and J. Wolfe, "C-band cross-polarization wind speed retrieval," *IEEE Geosci. Remote Sens. Lett.*, vol. 8, no. 3, pp. 456–459, May 2010.

[44] H. Shen, W. Perrie, Y. He, and G. Liu, "Wind speed retrieval from VH dual-polarization RADARSAT-2 SAR images," *IEEE Trans. Geosci. Remote Sens.*, vol. 52, no. 9, pp. 5820–5826, Sep. 2014.